


 Cite this: *RSC Adv.*, 2023, **13**, 16248

A novel n-p heterojunction $\text{Bi}_2\text{S}_3/\text{ZnCo}_2\text{O}_4$ photocatalyst for boosting visible-light-driven photocatalytic performance toward indigo carmine[†]

 Nguyen Thi Mai Tho, ^{*a} Nguyen Van Cuong, ^a Viet Ha Luu Thi, ^a Nguyen Quoc Thang, ^a and Phuc Huu Dang ^{*b}

An innovative p-n heterojunction $\text{Bi}_2\text{S}_3/\text{ZnCo}_2\text{O}_4$ composite was first fabricated via a two-step co-precipitation and hydrothermal method. By controlling the weight amount of Na_2S and $\text{Bi}(\text{NO}_3)_3$ precursor, different heterogeneous $x\text{Bi}_2\text{S}_3/\text{ZnCo}_2\text{O}_4$ were synthesized ($x = 0, 2, 6, 12$, and 20). The p-n heterojunction $\text{Bi}_2\text{S}_3/\text{ZnCo}_2\text{O}_4$ was characterized by structural, optical, and photochemical properties and the photocatalyst decoloration of indigo carmine. Mott–Schottky plots proved a heterojunction formed between n- Bi_2S_3 and p- ZnCo_2O_4 . Furthermore, the investigation of the photocurrent response indicated that the $\text{Bi}_2\text{S}_3/\text{ZnCo}_2\text{O}_4$ composite displayed an enhanced response, which was respectively 4.6 and 7.3 times ($4.76 \mu\text{A cm}^{-2}$) greater than that of the pure Bi_2S_3 ($1.02 \mu\text{A cm}^{-2}$) and ZnCo_2O_4 ($0.65 \mu\text{A cm}^{-2}$). Especially the optimized p-n $\text{Bi}_2\text{S}_3/\text{ZnCo}_2\text{O}_4$ heterojunction with 12 wt% Bi_2S_3 showed the highest photocatalyst efficacy of 92.1% at 40 mg L^{-1} solutions, a loading of 1.0 g L^{-1} , and a pH of 6 within 90 min of visible light illumination. These studies prove that p-n $\text{Bi}_2\text{S}_3/\text{ZnCo}_2\text{O}_4$ heterojunction photocatalysts can greatly boost their photocatalytic performance because the inner electric field enhances the process of separating photogenerated electron–hole pairs. Furthermore, this composite catalyst showed good stability and recyclability for environmental remediation.

Received 28th April 2023

Accepted 25th May 2023

DOI: 10.1039/d3ra02803h

rsc.li/rsc-advances

1. Introduction

Currently, environmental pollution in the world is at an alarming level, especially water pollution. Wastewater including pigments, reactive dyes, heavy metal ions, and organic substances is the main cause of pollution because it is difficult to decompose and highly resistant to light, heat, and oxidizing agents that can affect the health of humans and organisms.^{1,2} A typical indigo dye used in textile dyeing and other industries is indigo carmine ($\text{C}_16\text{H}_8\text{N}_2\text{Na}_2\text{O}_8\text{S}_2$). However, indigo carmine (IC) is a very dangerous agent that is categorized as being environmentally toxic; regular exposure to it can irritate the respiratory tract, the skin on the back of the eyes, and the cornea, in addition to causing acute toxicity. Therefore, the pollution control and treatment of IC dyes from textile dyeing wastewater are of great interest to many people.^{3–5} Over the past few years, advanced oxidation processes (AOPs) provide a possibility for completing the cleaning of wastewater polluted

with recalcitrant organic chemicals.⁶ A number of these methodologies are frequently employed in Advanced Oxidation Processes (AOPs), including (i) Fenton oxidations, (ii) photocatalysts, (iii) plasma oxidation, and (iv) ozonation. Recently, metal oxide semiconductor photocatalysis has been widely explored. WO_3 , TiO_2 , ZnO , Fe_2O_3 , ZrO_2 , CuO , and NiO are semiconductor photocatalysts.⁷ However, these metal oxide semiconductors only take advantage of the UV radiation spectrum (3–5% of the total solar spectrum) because of their wide bandgap.⁸ Moreover, hybrid metal chalcogenide compounds can have adequate redox potential while improving solar spectrum absorption.^{9–11} Among the hybrid metal chalcogenide compounds, n-type bismuth sulfide (Bi_2S_3), possesses unique properties such as wide light absorption, high dielectric properties, a narrow band gap (E_g) (approx. 1.3 eV), lamellar structure, and especially an adjustable band gap, so it is used in photocatalysis and photo electrochemistry (PEC).^{12–16} Unfortunately, the photogenerated electron–hole pair ($e_{\text{CB}}^- - h_{\text{VB}}^+$) recombines rapidly due to the narrow E_g of Bi_2S_3 , resulting in low separation efficiency and challenging its reality-based applications.⁶ So, scientists look for solutions such as dopants, decoration with the plasmonic noble metal, novel (p-n/n-n) heterojunction formation, etc.^{17–21}

^aFaculty of Chemical Engineering, Industrial University of Ho Chi Minh City, Ho Chi Minh, Vietnam. E-mail: nguyenthimaitho@iuh.edu.vn

^bFaculty of Fundamental Science, Industrial University of Ho Chi Minh City, Ho Chi Minh, Vietnam. E-mail: danghuuphuc@iuh.edu.vn

† Electronic supplementary information (ESI) available. See DOI: <https://doi.org/10.1039/d3ra02803h>



Recent research has focused on the transition metal p-type oxide ZnCo_2O_4 due to its narrow energy band, higher photoelectrochemical stabilization, higher electrical conductivity, and a larger amount of redox reaction sites than metal oxides (ZnO , Co_3O_4).^{22,23} It is noted that because of the specific energy band structure, the valence band (VB) is formed by the energy levels of O 2p, while the conduction band is formed by the energies of Co 3d. So, the electron inside the band gap can switch easily, thus increasing the photogenerated electron–hole lifetimes.²⁴ Besides, ZnCo_2O_4 is a promising candidate for fabricating an advanced p–n heterojunction in conjunction with other photocatalysts.²⁵ Some heterojunction structure was studied such as $\text{SnO}_2/\text{ZnCo}_2\text{O}_4$,²⁶ $\text{ZnCo}_2\text{O}_4/\text{Bi}_2\text{O}_3$,²⁵ $\text{ZnO}/\text{ZnCo}_2\text{O}_4$,²⁷ $\text{CaFe}_2\text{O}_4/\text{ZnCo}_2\text{O}_4$,²⁸ $\text{BiVO}_4/\text{ZnCo}_2\text{O}_4$ in the photo-degradation of dye molecules from aqueous solution.

Based on the above discussion, p–n heterojunctions structure including an n-type narrow bandgap Bi_2S_3 was deposited on the surface of p-type ZnCo_2O_4 , which is the solution to boost the photocatalyst efficacy of ZnCo_2O_4 . The structure with 12 wt% Bi_2S_3 on ZnCo_2O_4 showed an improvement in visible light photocatalytic performance than that of pure Bi_2S_3 and ZnCo_2O_4 . This is because ZnCo_2O_4 provides superior photoelectrochemical stability, whereas the low energy bandgap Bi_2S_3 boosts solar light absorption ability. The type-II heterojunction forms a built-in electric field between the interface of Bi_2S_3 and ZnCo_2O_4 semiconductors, which accelerates the separation of photocarriers and is good for applications related to energy harvesting. The process of degradation was thoroughly studied.

2. Experimental

2.1 Synthesis of ZnCo_2O_4

The ZnCo_2O_4 materials were fabricated by the coprecipitation method. A solution of 100 mL $\text{Zn}(\text{NO}_3)_2$ 0.1 M and 100 mL $\text{Co}(\text{NO}_3)_2$ 0.3 M with a $\text{Zn}^{2+}/\text{Co}^{2+}$ molar ratio of 1/3 was slowly added to 50 mL of 1 M NaOH with a rate of 10 mL min⁻¹. The solution was unchanged at pH 10 using NaOH and was stirred. The after-precipitation solution was aged at 105 °C for 15 hours. The resulting powders were filtered, cleaned with de-ionized water numerous times, and heated at 100 °C for 10 hours. The black powder was thermally treated at 600 °C for 4 h to receive ZnCo_2O_4 (ZC).

2.2 Synthesis of Bi_2S_3

The sample Bi_2S_3 was formed by slowly adding 10 mL Na_2S dissolved in ethylene glycol (EG) to 50 mL EG containing $\text{Bi}(\text{NO}_3)_3$, with a molar ratio of $\text{Bi}^{3+}/\text{S}^{2-}$ at 2/3. The Bi_2S_3 was collected, centrifuged, cleaned, and air-dried at 105 °C.

2.3 Synthesis of $\text{Bi}_2\text{S}_3/\text{ZnCo}_2\text{O}_4$ heterostructures

First, the as-prepared 0.5 g ZnCo_2O_4 and $\text{Bi}(\text{NO}_3)_3 \cdot 5\text{H}_2\text{O}$ which were diluted in a minimum amount of HNO_3 (5%) before being dispersed, were inserted into 50 mL of EG. The solution of 50 mL Na_2S with EG was added dropwise and slowly to the as-prepared solution. The suspension solution was stirred at 140 °C for 12 hours. Eventually, the $\text{Bi}_2\text{S}_3/\text{ZC}$ samples were

gathered following deionized water washing and 100 °C drying. By controlling the weight amounts of Na_2S and $\text{Bi}(\text{NO}_3)_3$, different $\text{Bi}_2\text{S}_3/\text{ZnCo}_2\text{O}_4$ heterogeneous were obtained (x is the mass percentage of $\text{Bi}_2\text{S}_3/\text{ZnCo}_2\text{O}_4$). Four samples are labeled as 2.0 $\text{Bi}_2\text{S}_3/\text{ZC}$; 6.0 $\text{Bi}_2\text{S}_3/\text{ZC}$; 12.0 $\text{Bi}_2\text{S}_3/\text{ZC}$ and 20.0 $\text{Bi}_2\text{S}_3/\text{ZC}$.

The obtained Bi_2S_3 , ZC, and $x.0\text{Bi}_2\text{S}_3/\text{ZC}$ powder were identified by X-ray diffraction (XRD), Fourier-transform infrared spectroscopy (FT-IR) microscopy (TEM), scanning electron microscopy (SEM), and X-ray photoelectron spectroscopy (XPS); the UV-visible diffuse reflectance spectrum (DRS); the energy dispersive X-ray (EDX), high-resolution electron microscope image (HRTEM), BET data including N_2 adsorption–desorption isotherms, inductively coupled plasma optical emission spectroscopy (ICP-OES), photocurrent response ($j-t$) and electrochemical impedance spectra (EIS). The ion Zn and Co leaching was detected by ICP-OES.

2.4 Evaluating photocatalytic performance

The catalytic activity of $x.0\text{Bi}_2\text{S}_3/\text{ZC}$ powder was evaluated based on the decomposition of IC dye ($\lambda_{\text{max}} = 612$ nm) using a 300 W halogen lamp (Osram, Germany). The catalytic reaction is carried out on a catalytic system consisting of two processes:

Adsorption processes: The adsorption–desorption equilibrium of indigo carmine on the surface of $x.0\text{Bi}_2\text{S}_3/\text{ZC}$ catalysts was in the dark for 1 hour.

Degradation processes: The light source is turned on to perform the photocatalytic reaction for 90 min. After every 15 minutes, 5 mL of suspension is placed in the centrifuge system to remove the catalyst. The solution was stirred using a magnetic stirrer and circulating water to keep the room temperature. The ultraviolet-visible spectrophotometer determines the concentration of the IC solution.

3. Results and discussion

3.1 Characterization

The structure of the prepared catalyst is studied based on XRD spectroscopy (Fig. 1a). The strong and sharp diffraction peaks of ZC at 31.85°; 36.17°; 47.38°, 56.76°, 62.77°, and 67.67° ascribed with (220); (311); (400); (422); (511) and (440) lattice planes of homogeneous cubic spinel phase ZnCo_2O_4 (JCPDS no. 23-1390), proving that the ZC was successfully synthesized by coprecipitation method. The diffraction peaks of pure Bi_2S_3 at 2θ values 22.46; 25.12; 28.35, 31.71; 39.8; 45.3; 46.5; 58.7 coincide with the orthorhombic Bi_2S_3 phase (JCPDS no. 17-0320).²⁹ The XRD patterns of $x.0\text{Bi}_2\text{S}_3/\text{ZC}$ heterostructures ($x = 2, 6$) are similar to those of ZC and do not appear to have diffraction peaks of pure Bi_2S_3 . This can be caused by the low loading weight of Bi_2S_3 on ZC. However, $x.0\text{Bi}_2\text{S}_3/\text{ZC}$ ($x = 12, 20$) heterostructures appear as main diffraction peaks of Bi_2S_3 the intensities of them increase according to the content percentage of Bi_2S_3 on heterostructures increasing. The above results suggest that the $x.0\text{Bi}_2\text{S}_3/\text{ZC}$ heterostructures were successfully synthesized with good crystallinity and less impurity.

The FTIR spectra of Bi_2S_3 , ZC, and $x.0\text{Bi}_2\text{S}_3/\text{ZC}$ heterostructure are presented in Fig. 1b. The Bi_2S_3 sample exhibited



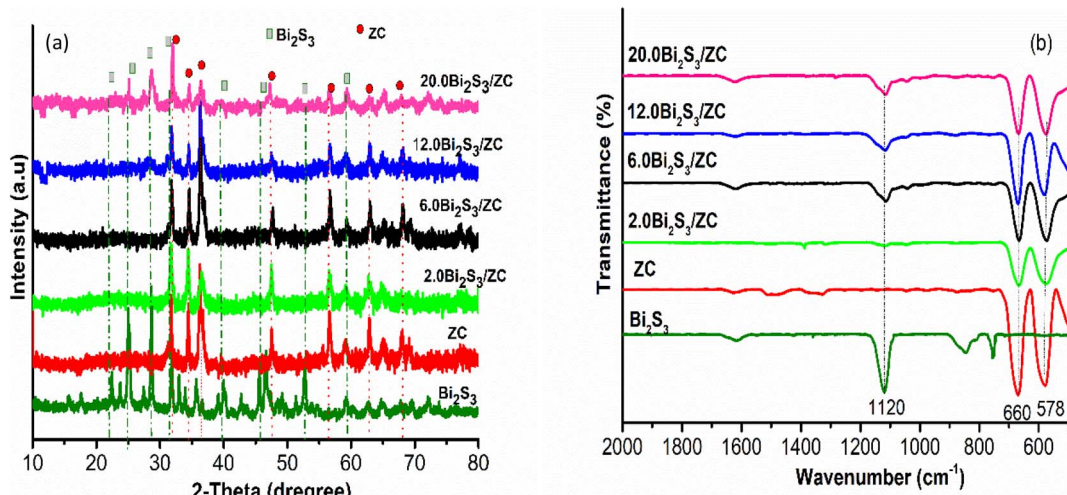


Fig. 1 XRD (a), FTIR (b) patterns for the Bi₂S₃, ZC, and x.0Bi₂S₃/ZC (x = 2, 6, 12, 20).

characteristic vibrational peaks at 1120 cm⁻¹ relating to the stretching modes Bi-S groups.³⁰ For x.0Bi₂S₃/ZC samples characteristic bands of the stretching modes Bi-S are also observed at 1120 cm⁻¹ and this indicates the presence of Bi₂S₃ in the composites. This peak was observed with lower intensities in the composites which indicates the formation of x.0Bi₂S₃/ZC heterojunction nanocomposites. In addition, the characteristic peaks of the ZC and x.0Bi₂S₃/ZC (x = 2, 6, 12, 20) are observed in 660 cm⁻¹ and the range of 578 cm⁻¹ which are metal-oxy vibration such as the Co-O tensile and the Zn-O spinel.³¹

In Fig. 2a, the synthesized Bi₂S₃ was clearly shown to produce nanoparticles with a homogeneous array, and porous material. Bi₂S₃ nanoparticles aggregated loosely, and there were apparent pores, indicating that adding additional active sites might boost

catalytic activity. Many ZC layers were stacked resulting in typical nanoplates with a homogeneous array with thin sheets. FESEM image of x.0Bi₂S₃/ZC shows that Bi₂S₃ are precipitated and wrapped on the surface of ZC. Nanoparticles of Bi₂S₃ were coated on a surface of ZC, forming a heterogeneous interface with intimate contact. The more Bi₂S₃ content, the better x.0Bi₂S₃/ZC nanosheets become rough and irregular gradually.

In addition, the HRTEM results also confirmed the formation of the 12.0Bi₂S₃/ZC heterojunction. The lattice fringes were approximately ~0.310 nm which is ascribed to the (221) plane of orthorhombic Bi₂S₃,^{32,33} in which 0.239 nm belongs to the (311) plane of cubic spinel ZC.^{23,28} In addition, the TEM image also observed the appearance of an amorphous phase at the interface of the crystalline Bi₂S₃ and ZC phases. The association

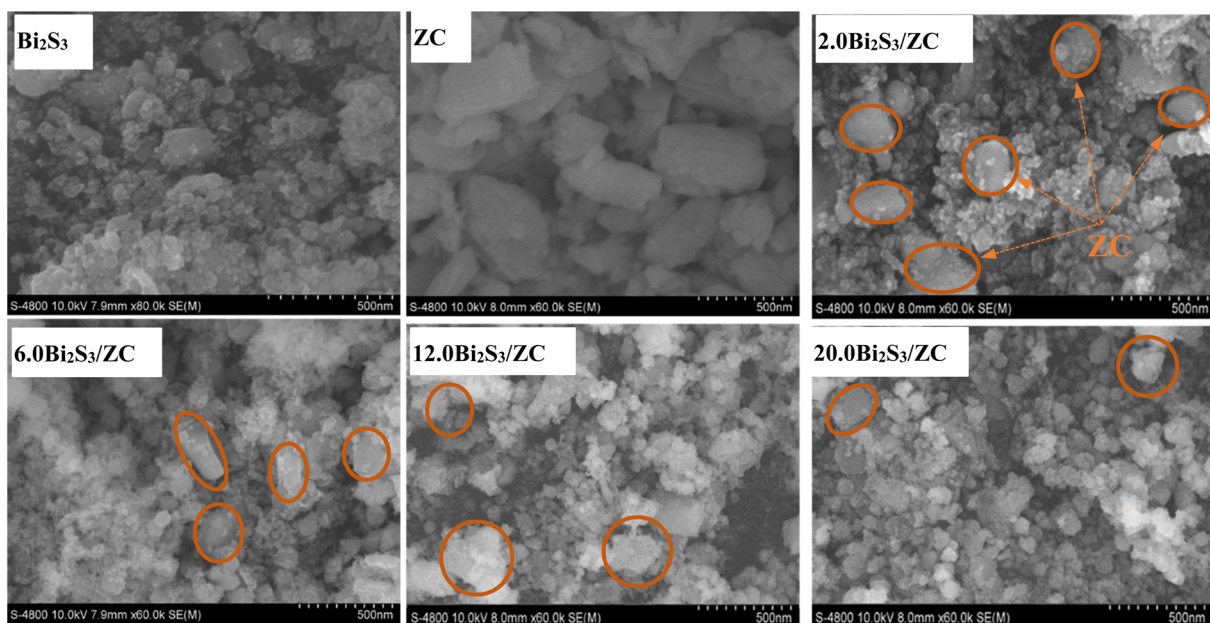


Fig. 2 The FESEM images of Bi₂S₃, ZnCo₂O₄ and x.0Bi₂S₃/ZC (x = 2, 6, 12, 20).



between the crystalline and amorphous phases helps speed up the charge migration due to the mobility of localization sites in the amorphous phase.³⁴ The distribution of particles was around 20-60 nm, which was determined by the TEM image (Fig. S1†). Moreover, Fig. 3c and d displays that the EDX spectra of ZC consists of only three main elements Zn (19.04%), Co (23.01%), O (57.94%) while the 12.0Bi₂S₃/ZC heterojunction shows the presence of Zn (28.93%), Co (7.18%), O (57.59%), Bi

(1.47%) and S (4.82%). This result proved the formation of the Bi₂S₃/ZC heterojunction. Furthermore, the Co/Zn atomic ratio in ZC and 12.0Bi₂S₃/ZC are about 2.17 and 2.3 by ICP-OES measurement, respectively (Table S1†).

The optical absorption of Bi₂S₃, ZC, and x Bi₂S₃/ZC are shown in Fig. 4b. ZC shows good absorbance of light located at about 500 nm while pure Bi₂S₃ presents an optical absorption edge nearly in the visible light spectral region that extended even

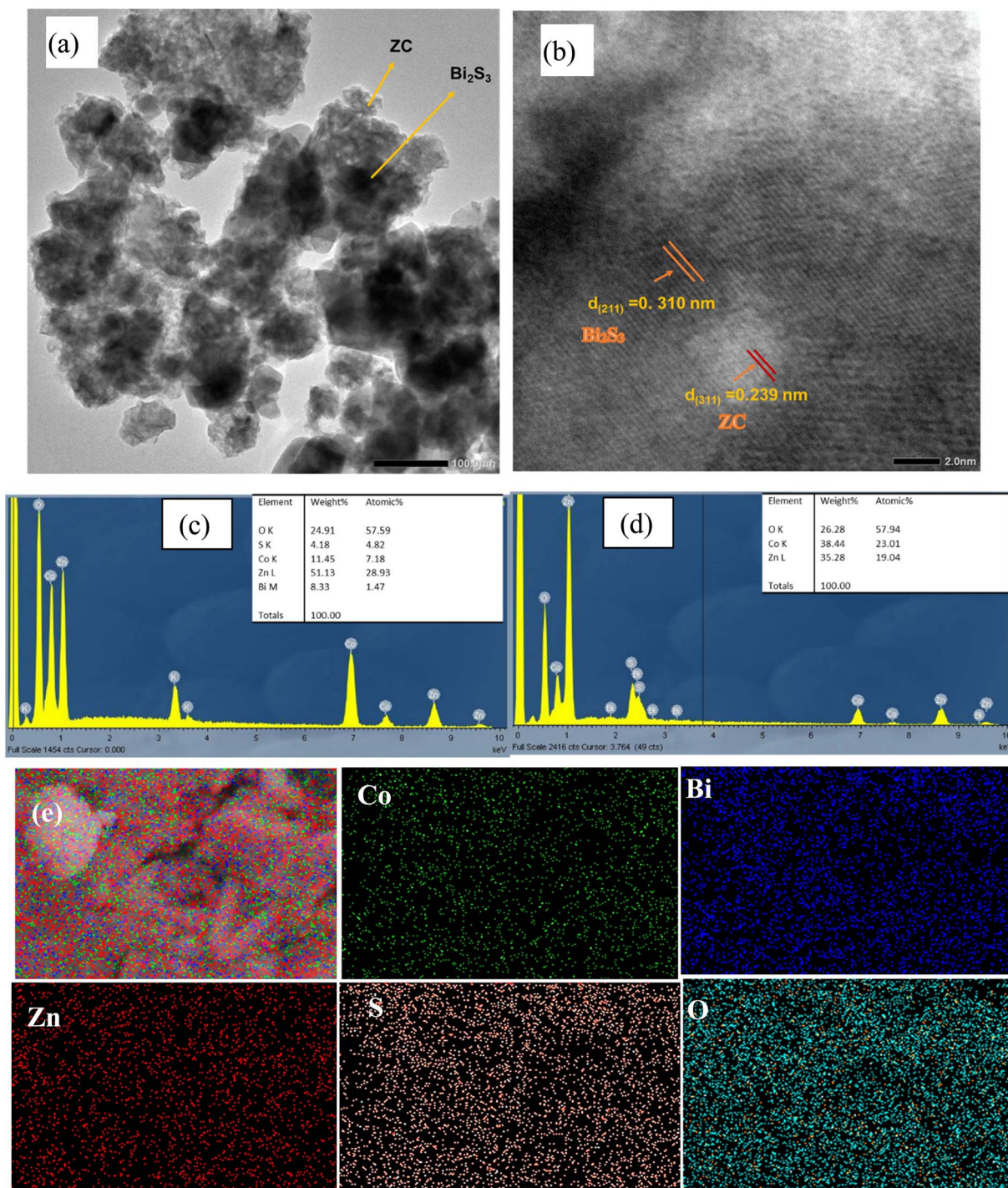


Fig. 3 TEM (a) and HRTEM (b) diagram of 12.0Bi₂S₃/ZC samples; the EDX (c–e) of ZnCo₂O₄ and 12.0Bi₂S₃/ZC samples.



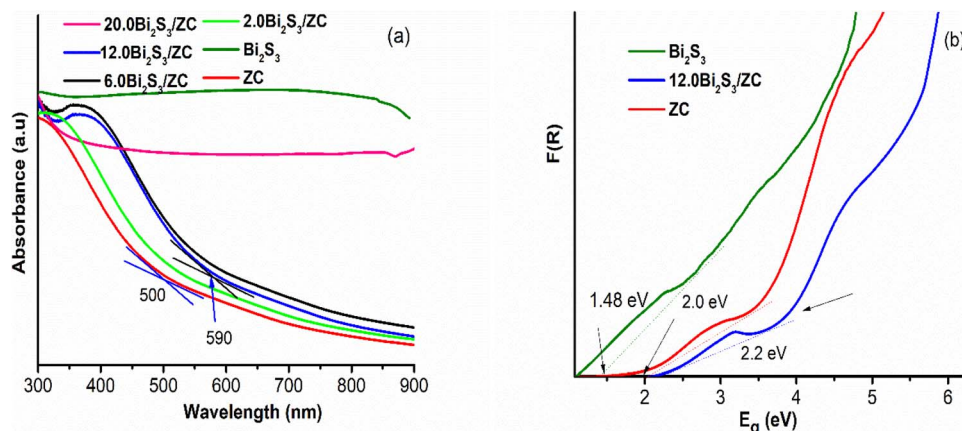


Fig. 4 (a) UV-vis DRS spectra, (b) band gap energies of ZC and Bi₂S₃.

to the infrared region. For the x .0Bi₂S₃/ZC heterojunction, the absorption edges have changed compared to ZC, edges appeared at 590 nm and were blue-shifted in comparison with those of ZC. It has been discovered that the proportion of the amount of Bi₂S₃ causes a change in the absorption edge and absorbance density in the visible spectrum. However, the band gap of 20.0Bi₂S₃/ZC will be dominated by the narrower band gap of Bi₂S₃ because Bi₂S₃ covers the surface of ZC. This phenomenon was observed in the morphology image FESEM. Besides, Using the Kubelka-Munk function estimate the band gap energy of the powders. Results can be seen from Fig. 4b that the bandgap of ZC, Bi₂S₃, and 12.0Bi₂S₃/ZC are approximately 2.2 eV, 1.48 eV, and 2.0 eV, respectively. The development of Bi₂S₃ nanoparticles on the surface of ZC can interface in heterojunction which increases more photogenerated hole-electron pair, thereby enhancing the photocatalytic performance of 12.0Bi₂S₃/ZC.^{26,27}

The elements and chemical states in photocatalyst heterojunction were studied by X-ray photoelectron spectroscopy (XPS). As depicted in Fig. 5a Zn, Co, O, and S elements of both ZnCo₂O₄ and x .0Bi₂S₃/ZC were detected from characteristic peaks of O 1s; Co 2p and Zn 2p; x .0Bi₂S₃/ZC samples also have characteristic peaks of S 2p and Bi 4f.²² The high-resolution spectrum for the S 2p and Bi 4f region shows (Fig. 5b) the number of deconvoluted peaks at 158.16 and 163.71 eV ascribed to Bi 4f_{7/2} and Bi 4f_{5/2} orbital, meanwhile, the peak at 161.22 eV and 162.64 eV can be ascribed to S 2p_{3/2} and S 2p_{1/2}.^{32,35} The first group at 779.37; 794.47 eV and the second group at 780.61; 795.88 eV binding energy (Fig. 5c) which can be ascribed to Co 2p in ZC indicating that the valence of Co³⁺ and Co²⁺ of ZC spinel, these peaks move to the direction of large binding energy with 780.53; 796.55 eV and 783.12; 802.14 eV in 12.0Bi₂S₃/ZC, respectively.³⁶ Moreover, a multivalent in ZC was observed by the two weaks satellite peaks, as mentioned in the literature. Fig. 5d shows the peaks of ZC are Zn 2p_{3/2} (1021.38 eV) and Zn 2p_{1/2} (1044.45 eV), respectively. Moreover, the existence of Zn²⁺ in the ZC structure was identified by the distance between two peaks Zn2p_{3/2} and Zn2p_{5/2} (23.07 eV). Besides, the shift of Zn2p orbitals peaks to the higher binding energies for the 12.0Bi₂S₃/ZC heterojunction, compared to ZC. The

deconvolution O 1 s peak (Fig. 5e) using the Gaussian-based included 530.48 and 532.65 components, which were attributed to metal–oxygen bonds (O₂[−]), the surface hydroxyl groups, and the O–H species absorbed water on the surface of ZC.³⁷ The positive shift of binding energy of O 1s for 12.0Bi₂S₃/ZC heterojunction compared to ZC indicates a change of the electron density, establishing an effective charge transfer between ZC and Bi₂S₃. This could be explained due to the interaction effect of the strong chemical bond between ZC and Bi₂S₃ changing the outer electron cloud densities of Co.^{22,25,36} Finally, from the XPS results, we can conclude the 12.0Bi₂S₃/ZC photocatalyst contains the elements Bi, S, O, Co, and Zn, indicating that Bi₂S₃ was synthesized successfully and loaded on the surface of spinel phase ZnCo₂O₄ nanoparticles.

Fig. 6 shows the result of the N₂ adsorption/desorption isotherm and pore-size distribution of ZC and 12.0Bi₂S₃/ZC that all samples exhibited a type IV isotherm, and the hysteresis loops were the type of H3. The specific surface area, pore volume, and average pore size of the ZC and 12.0Bi₂S₃/ZC were shown in Table 1. The Specific surface area calculated from the Brunauer–Emmett–Teller (BET) isotherms is 15.49 m² g^{−1} and 21.33 m² g^{−1} for ZC and 12.0Bi₂S₃/ZC, respectively. The increased surface area of 12.0Bi₂S₃/ZC could be attributed to the loading of pores Bi₂S₃ nanoparticles. The pore size distribution of ZC is approximately 13.07 nm, while that of 12.0Bi₂S₃/ZC is 15.76 nm. The significant specific surface area and pore constructed help increase active sites, enhance organic dye adsorption, and effectively transfer charge carriers, thus enhancing the photocatalytic activity of 12.0Bi₂S₃/ZC.

3.2 Photoelectrochemical performance

The photoelectrochemical operation of the x .0Bi₂S₃/ZC in 0.5 M Na₂SO₄ solution was investigated to determine the separation and charge transfer efficiency. The photoelectrochemical efficiency of Bi₂S₃, ZC, and 12.0Bi₂S₃/ZC is shown in Fig. 7. Transient photocurrent response was tested in all samples (On and off interval time being 10 s). According to the transient photoelectric response (I - t curve) in Fig. 6a, the 10%-Bi₂S₃/ZC composite has a greater photocurrent intensity (4.76 μ A cm^{−2})



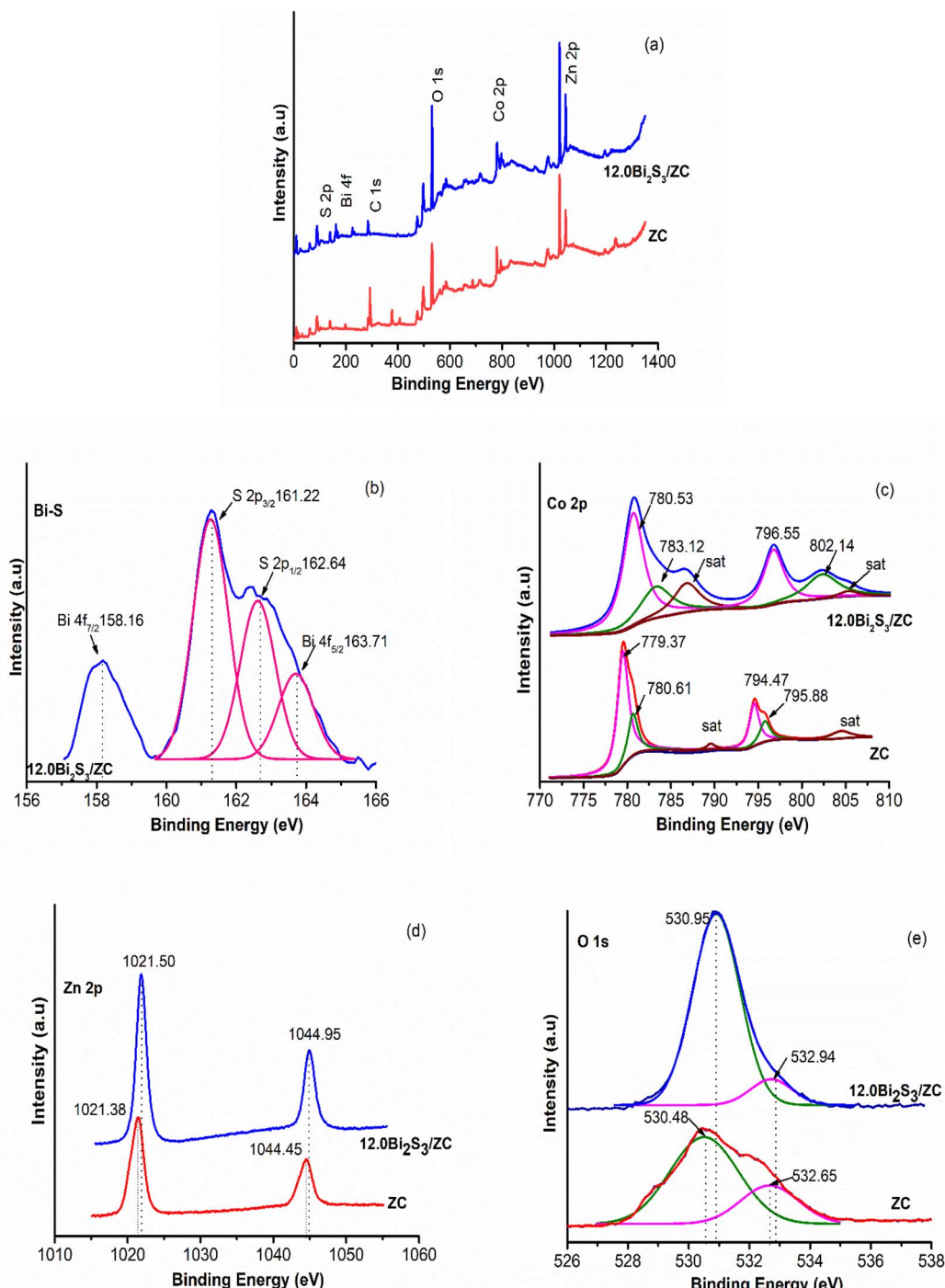


Fig. 5 XPS spectra (a) survey; (b) Bi-S 2p; (c) Co 2p; (d) Zn 2p; (e) O 1s of pristine ZnCo_2O_4 and $12.0\text{Bi}_2\text{S}_3/\text{ZC}$ samples.

than the pure Bi_2S_3 ($1.02 \mu\text{A cm}^{-2}$) and ZC ($0.65 \mu\text{A cm}^{-2}$). It is generally agreed that the separation of photogenerated charges is more effective, and its photocatalytic performance is the greater intensity of photocurrent.^{35,38,39} Moreover, when the lamp is switched on, the photocurrent of $12.0\text{Bi}_2\text{S}_3/\text{ZC}$ continually rises, showing that the photogenerated electron–hole pairs separate continuously.

Electrochemical impedance spectroscopy (EIS) experiments correlate the charge transport resistance of a catalyst with the

Nyquist plot, where a significant shift in the arc radius of the Nyquist plot indicates effective charge transport in the preparation of Bi_2S_3 – ZC. EIS of synthesized catalysts is displayed in Fig. 7b, and the equivalent circuit is shown in the upper right corner of Fig. 7b. Pure Bi_2S_3 , ZC, and $12.0\text{Bi}_2\text{S}_3/\text{ZC}$ samples all have R_s values of 2627, 3012, and 1794Ω , whereas the corresponding R_{ct} values are 43.34, 53.84, and 42.04Ω . There is less resistance to charge transfer and more efficient carrier transfer when the semicircle's radius is smaller.^{40,41} It can be observed

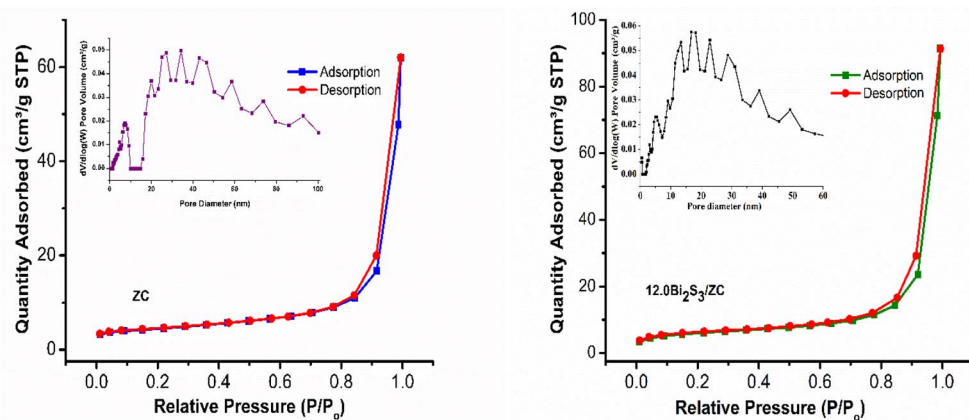


Fig. 6 Nitrogen adsorption–desorption isotherm and Barrett–Joyner–Halenda (BJH) pore-size distribution (a) ZC and 12.0Bi₂S₃/ZC.

Table 1 The specific surface area, pore volume, and average pore size of the ZC and 12.0Bi₂S₃/ZC

Sample	S_{BET} (m ² g ⁻¹)	Pore volume (cm ³ g ⁻¹)	Average pore size (nm)
ZC	15.49	0.03566	13.07
12.0Bi ₂ S ₃ /ZC	21.33	0.04342	15.76

from the specific resistance values that the 12.0Bi₂S₃/ZC has the lowest resistance value, is more photo-catalytically active, and outperforms pure Bi₂S₃ and ZnCo₂O₄ in terms of surface charge transfer abilities. The EIS finding agreed with those from the UV-DRS characterization research and photocatalytic measurements.

The semiconductor and energy-gap structure of the photocatalyst was analyzed using the Mott–Schottky (M–S) measurement at 1000 Hz in 0.5 M Na₂SO₄ solution at pH 7. The acquired curve for ZnCo₂O₄ has a negative slope, suggesting that it is an n-type semiconductor, whereas the obtained curve for Bi₂S₃ has a positive slope, showing that it is a p-type semiconductor (see Fig. 7c). This study reveals that the CB potential of Bi₂S₃ and the VB potential of ZnCo₂O₄ are identified at -0.355 V vs. NHE and 1.535 V vs. NHE ($E_{\text{NHE}} = E_{\text{Ag/AgCl-3.5M}} + 0.24$), respectively. With the aforementioned results, it has been determined that the VB of Bi₂S₃ and CB of ZnCo₂O₄ are approximately 1.125 V and -0.665 V, respectively, as calculated by the formula $E_{\text{CB}} = E_{\text{VB}} - E_{\text{g}}$. To understand the mechanism of photocatalysis in the Bi₂S₃/ZnCo₂O₄ heterojunction, an M–S plot has been measured. The results indicate a flat band potential shift positive for the Bi₂S₃/ZnCo₂O₄ heterostructure photocatalyst, suggesting the formation of a p-ZC/n-Bi₂S₃ heterojunction. This finding is supported by previous research.^{1,42}

3.3 Photocatalytic activity

3.3.1 Effect of a percentage of Bi₂S₃ in Bi₂S₃/ZC heterojunction. Fig. 8a and b displays the results of evaluating the photocatalytic activity of x .0Bi₂S₃/ZC catalysts ($x = 2, 6, 12, 20$) on the IC degradation process.

After a 60 minutes absorption process, the quantity of IC dye adsorbed from 29–33% for the adsorption equilibrium while after 90 minutes under the degradation process, the amount of IC degraded from 67% to 92.1% by x .0Bi₂S₃/ZC. The x .0Bi₂S₃/ZC heterostructures exhibit significantly increased photocatalytic performance as compared with ZC. The photodegradation efficiency of IC reached 92.1% for 12.0Bi₂S₃/ZC and only 53.8% for ZC. The photocatalytic experimental results of x .0Bi₂S₃/ZC obey the pseudo-first-order kinetic as indicated by the good values of the correlation coefficient ($R^2 > 0.9588$). The photocatalyst performance was determined by the values of k , which were subsequently arranged in descending order of 12.0Bi₂S₃/ZC (0.0230 min⁻¹) $>$ 6.0Bi₂S₃/ZC (0.0158 min⁻¹) $>$ 2.0Bi₂S₃/ZC (0.0126 min⁻¹) $>$ 20.0Bi₂S₃/ZC (0.00828 min⁻¹) $>$ ZC (0.00499 min⁻¹) $>$ Bi₂S₃ (0.0042 min⁻¹).

The photocatalytic activity of x .0Bi₂S₃/ZC heterostructures was affected by Bi₂S₃ content. The photocatalytic activity of x .0Bi₂S₃/ZC heterostructures first increased and then decreased with increasing Bi₂S₃ content. The interaction between Bi₂S₃ and ZC boosts that improve the efficiency of charge separation, because of the contribution of the internal electric field between the junction surface between Bi₂S₃ and ZC. However, for the 20.0Bi₂S₃/ZC sample, the catalytic efficiency decreased markedly because the amount of Bi₂S₃ completely covered the ZC surface, leading to the loss of the number of light photons in the visible light region. This agrees with the UV-Vis DRS spectra and FESEM image.²⁶

The amount of 0.5 – 2.0 g L⁻¹ 12.0Bi₂S₃/ZC influence on photocatalytic degradation of IC was studied with unchanged the concentration of IC at 40 mg L⁻¹ at pH 6.0 (Fig. 8c). When the loading of 12.0Bi₂S₃/ZC was changed from 0.5 to 1.0 g L⁻¹, the rate constant k of IC degradation increased significantly from 0.0068 to 0.0230 min⁻¹. However, the degradation efficiency decreases from 77.4% ($k = 0.0121$ min⁻¹) to 72% ($k = 0.0067$ min⁻¹) with catalyst loading of 1.5 – 2.0 g L⁻¹. The above results can be explained as follows: the overall amount of photon absorption and activity centers on the surface of the catalyst increases with increasing the catalyst loading. However, the catalyst loading considerably increases, and the increased



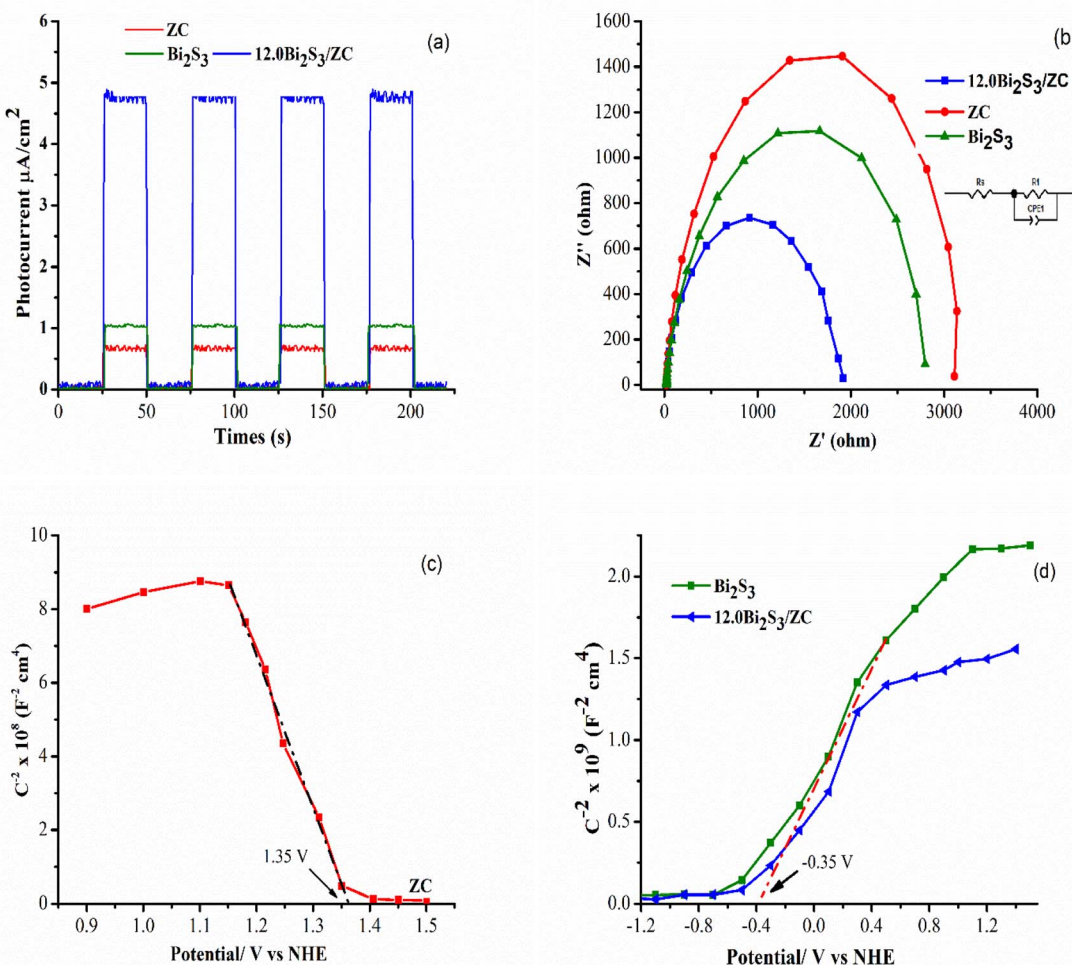


Fig. 7 (a) Transient photocurrent response; (b) EIS curves, (c and d) Mott–Schottky plot of ZC, 12.0Bi₂S₃, and 12.0Bi₂S₃/ZC.

turbidity prevented light transmission into the solution, thereby decreasing the activity of the catalyst.^{43,44}

3.3.2 Effect of initial IC concentration. The photocatalytic activity of 12.0Bi₂S₃/ZC powder (1.0 g L⁻¹) was studied with various initial IC concentrations (20 to 50 mg L⁻¹) at pH 6 (Fig. 8d). The results showed that as the initial IC concentration changed from 20 to 50 mg L⁻¹, the degradation rate reduced from 0.661 to 0.162 min⁻¹. This reduces the number of photo-generated photons by obstructing the passage of light into the solution and onto the catalyst surface. As a result, there are fewer OH radicals formed on the surface, which reduces the process of IC decomposition.⁴³

3.3.3 Effect of initial pH value. The degradation process of 40 mg L⁻¹ IC of 1.0 g L⁻¹ catalyst 12.0Bi₂S₃/ZC was studied in pH ranges 4; 6; 8 (Fig. 9a). Following 90 minutes of visible light, the percentages and rate constant *k* of IC degradation at pH 4.0, 6.0, and 8.0 were 78.5% (*k* = 0.0138 min⁻¹), 92.1% (*k* = 0.0230 min⁻¹), 61.3% (*k* = 0.0076 min⁻¹), respectively, shown in Fig. 9. As pH_{pzc} 6.4 of 12.0Bi₂S₃/ZC > pH 4, and pH 6 of the solution, the surface of the catalyst gets positively charged. Consequently, electrostatic attraction between the negative charge of IC dye in solution and the positively charged 12.0Bi₂S₃/ZC catalyst surface leads to the

increase of photocatalytic degradation. However, the degradation efficiency of IC at pH 4 is lower than that at pH 6 due to the large concentration of H⁺, which hinders the attractive interaction between anion IC⁻ and the 12.0Bi₂S₃/ZC catalyst surface. While pH_{pzc} < pH 8, the electrostatic repulsion between the anionic IC solution and the negatively charged catalyst surface appears, thereby restricting the decomposition of the IC.^{7,45}

3.3.4 Stability and reusability. The photochemical stability of 12.0Bi₂S₃/ZC (Fig. 9b) was tested with the initial IC concentration of 30 mg L⁻¹, pH 6.4, and the loading catalyst of 1.0 g L⁻¹ under the presence of visible light. The used catalyst was centrifuged into distinct components before being cleaned with deionized water and heated at 110 °C. The IC dye degradation efficiency after six consecutive reuses was 92.10%; 91.30%; 89.8%, 87.90%; 83.3 and 78.1%. This indicates that the 12.0Bi₂S₃/ZC was good stability and recyclability. Besides, the concentration of Zn and Co ion leaching was found 0.148 and 0.06 mg L⁻¹ in the solution after six cycles. The results suggest that the utilization of Bi₂S₃ nanoparticles as a support material improves the durability of ZnCo₂O₄ catalysts. The amount of total organic carbon (COD) in the initial solution, start and end of light irradiation were fixed at pH 6.0, using 12.0Bi₂S₃/ZC with a catalyst/IC solution ratio of

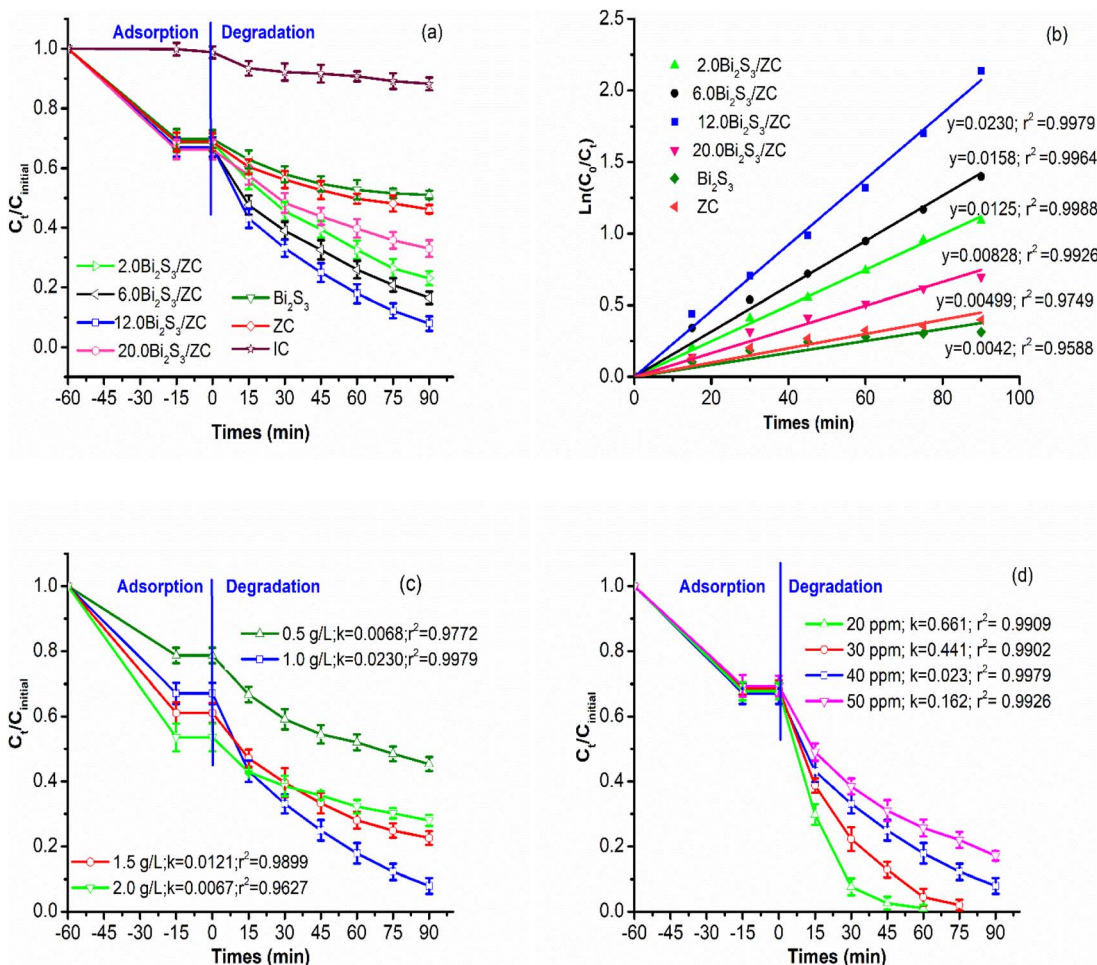


Fig. 8 (a and b) Effect of percentage of Bi_2S_3 in $\text{Bi}_2\text{S}_3/\text{ZC}$ heterojunction (the mass percentage of $\text{Bi}_2\text{S}_3/\text{ZnCo}_2\text{O}_4$ = 2.0, 12.0, 16.0, 20.0, loading of $\text{Bi}_2\text{S}_3/\text{ZnCo}_2\text{O}_4$ = 1.0 g L⁻¹, pH 6, C_{initial} = 40 ppm); (c) effect of the loading of 12.0 $\text{Bi}_2\text{S}_3/\text{ZC}$ (0.5–2.0 g L⁻¹ of 12.0 $\text{Bi}_2\text{S}_3/\text{ZC}$, pH 6, C_{initial} = 40 ppm); (d) effect of initial IC concentration (C_{initial} = 20–50 ppm, pH 6, loading of 12.0 $\text{Bi}_2\text{S}_3/\text{ZnCo}_2\text{O}_4$ = 1.0 g L⁻¹); effect of the loading of 12.0 $\text{Bi}_2\text{S}_3/\text{ZC}$.

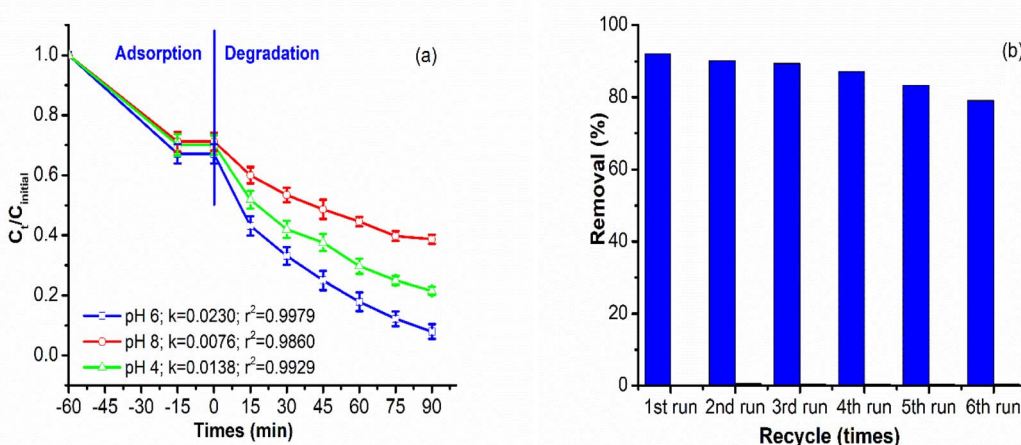


Fig. 9 (a) Effect of Initial pH value (pH 4–8, loading of 12.0 $\text{Bi}_2\text{S}_3/\text{ZnCo}_2\text{O}_4$ = 1.0 g L⁻¹, C_{initial} = 40 ppm); (b) stability and reusability.

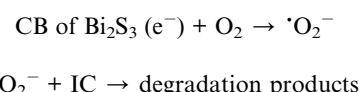
1.0 g L⁻¹, were approximated to be about 74.256; 66.766 mg L⁻¹ and 17.358 respectively. The COD removal efficiencies were achieved at about 10.1%; 86.05% start and end of 90 min visible light irradiation time. IC was completely mineralized to CO₂ and H₂O by photocatalytic degradation.

3.3.5 Effects of different scavengers. The main active species related to 12.0Bi₂S₃/ZC photocatalytic degradation of IC was studied. Scavengers were used as ethanol 0.5 M, disodium-methylene dianacetate (Na₂EDTA) 0.01 M, and *p*-benzoquinone 0.025 mM, were used as 'OH, h⁺ and 'O₂⁻, respectively. As evident from Fig. 10, the degradation performance decreased in the order: of no quencher > ethanol > Na₂EDTA > *p*-benzoquinone. As observed, only approximately 55% (with $k = 0.0046 \text{ min}^{-1}$) and 50% (with $k = 0.0056 \text{ min}^{-1}$) of the IC were degraded when *p*-benzoquinone and Na₂EDTA were added to the system. The experiments indicated that the generated 'O₂⁻ radicals and h⁺ were the dominant active species than OH⁻ radicals in the photocatalytic degradation of IC.

3.3.6 Possible photocatalytic mechanism. The diagram in Fig. 11 illustrates the suggested photocatalytic mechanism of the 12.0Bi₂S₃/ZC photocatalyst heterojunction. Before contact, p-type ZC has a Fermi level lower than those for n-type Bi₂S₃, so, electron directional diffusion from the Fermi level of n-type Bi₂S₃ to the Fermi level p-type ZC due to different Fermi levels. On another side, the hole diffused from VB of ZC to VB of Bi₂S₃ at the interface junction area. As a result, a depletion area was formed between the interface of ZC and Bi₂S₃ which accumulated negative charges on the ZC side and positive charges in Bi₂S₃. The Fermi level of Bi₂S₃ shifted downward while the Fermi level of ZC upward, to attain the equilibration. As mentioned above, a flat band potential of the Bi₂S₃/ZnCo₂O₄ heterostructure photocatalyst has shifted positively.

n-Bi₂S₃ nanoparticles warped on the ZC nanosheet formed a significant amount of interfacial sites, allowing for easy migration of the photoinduced charge carriers through the junction from one side to another. After contact, the Fermi level between p-ZC and n-Bi₂S₃ was equal, 12.0Bi₂S₃/ZC heterojunction generated

electrons and holes pair at both CB and VB of ZC and Bi₂S₃ under light illumination. The movement of photogenerated electrons from the CB of ZnCo₂O₄ to the CB of Bi₂S₃ is facilitated. This result agrees with XPS, Co2p peak of 12.0Bi₂S₃/ZC shift to higher binding compared to ZC due to electron cloud density in ZC decrease. In particular, the internal electric field region is formed at the interface of the junction, which is accelerated and separated whole photoexcited electron-hole charge pairs, and that restricted the possibility of a photogenerated charge carrier recombining. This transfer leads to an increase in richer electrons in the CB of Bi₂S₃. The CB electrons of Bi₂S₃ are capable of reacting with O₂ absorbed on the surface, resulting in the production of the one-electron reduction of dioxygen O₂ such as superoxide radical anion ('O₂⁻). This is because CB Bi₂S₃ has a greater negative potential than O₂/'O₂⁻ (-0.33 V vs. NHE),^{46,47} as follows;



In addition, the holes of Bi₂S₃ migrate towards the VB of ZnCo₂O₄ with the helpful support of a built-in electric field for can directly decompose IC.^{25,43} The decoloration of IC can also be contributed by the remaining holes (h⁺) at the VB of Bi₂S₃.^{30,33}

The reasons why Bi₂S₃/ZC heterostructure shows excellent photocatalyst performance are as follows: (i) the Bi₂S composite with ZnCo₂O₄ improved photon absorption; (ii) an n-p heterojunction constructs inner built-in potential at the interface between Bi₂S₃ and ZC. Consequently, an increased quantity of free charges accumulates at the junction, as proven by the M-S tests; (iii) the HRTEM image demonstrates that the Bi₂S₃ amorphous layer, which is deposited onto the ZnCo₂O₄ structure, functions as a catalyst that enables charge injection, thus generating more photogenerated pathways. This is a critical factor in enhancing the activity of the photocatalyst. Therefore, the heterostructure formed between Bi₂S₃ and ZC exhibits

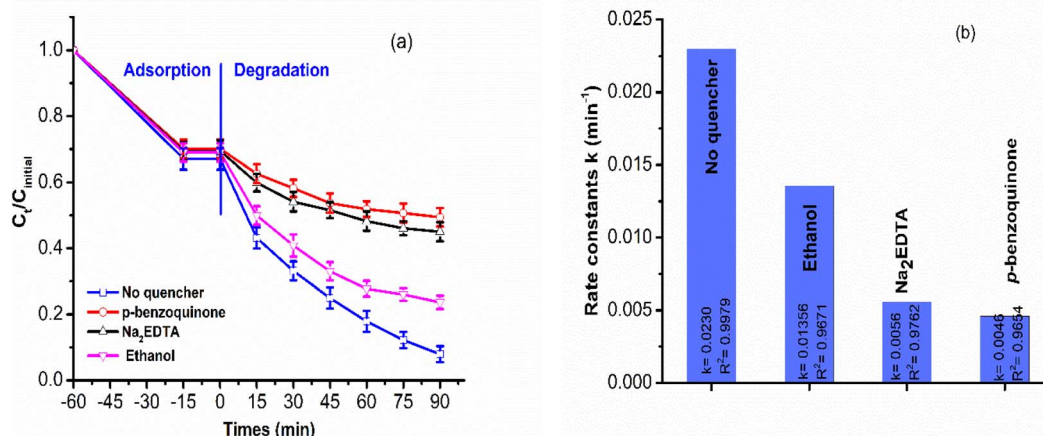


Fig. 10 (a and b) Effects of different scavengers on indigo carmine degradation over 12.0Bi₂S₃/ZC.



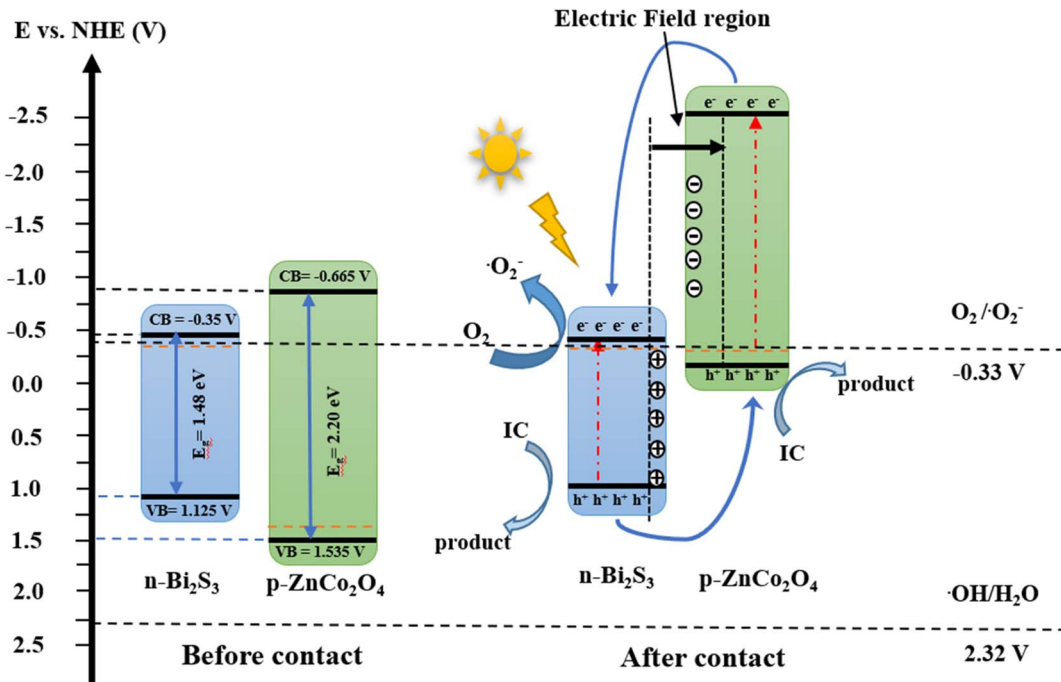


Fig. 11 Possible photocatalytic mechanism.

potential as a photocatalyst for the decomposition of diverse water pollutants in the presence of natural sunlight.

4. Conclusion

In summary, p-n heterojunction $x.0\text{Bi}_2\text{S}_3/\text{ZC}$ ($x = 1, 2, 6, 12, 20$) photocatalysts were successful. The chemical structure, morphology, optical, and photoelectrical properties of $x.0\text{Bi}_2\text{S}_3/\text{ZC}$ powder were analyzed. By controlling the molar amounts of Na_2S and BiNO_3 , we have found that the Bi_2S_3 modification can tremendously boost the photocatalytic performance of ZC. When compared to pure ZC, the self-biased photocurrent density of $12.0\text{Bi}_2\text{S}_3/\text{ZC}$ is 7.3 times higher. The EIS results offer enhanced comprehension of the function participated by Bi_2S_3 in the efficient separation and transfer of photogenerated charge carriers due to the contribution of an internal electric field. The results find that the $12.0\text{Bi}_2\text{S}_3/\text{ZC}$ showed a higher efficiency of photodegradation than that of ZC and Bi_2S_3 for the degradation of IC and the degradation rate is 5 times higher than that of ZC. A pseudo-first-order kinetics equation is perfectly suitable for the IC decomposition of an $x.0\text{Bi}_2\text{S}_3/\text{ZC}$ catalyst. Additionally, the results of different scavengers indicated that the important active species for IC decomposition were $\text{O}_2^{\cdot-}$ and h^+ .

Author contributions

Nguyen Thi Mai Tho: methodology, writing – original draft, validation, writing – review & editing, project administration. Nguyen Van Cuong: investigation, resources. Luu Thi Viet Ha: data curation, software. Nguyen Quoc Thang: investigation, resources. Dang Huu Phuc: writing – review & editing.

Conflicts of interest

The authors declare that they have no known competing interests that could have appeared to influence the work reported in this paper.

Acknowledgements

This work is supported by Industrial University of Ho Chi Minh City (IUH), Ho Chi Minh, Vietnam under grant number 22/1HH01.

References

- 1 S. Wang, T. He, J. Yun, Y. Hu, M. Xiao, A. Du and L. Wang, *Adv. Funct. Mater.*, 2018, **28**, 1802685.
- 2 S. Lodha, A. Jain and P. B. Punjabi, *Arabian J. Chem.*, 2011, **4**, 383–387.
- 3 M. N. Chong, B. Jin, C. W. K. Chow and C. Saint, *Water Res.*, 2010, **44**, 2997–3027.
- 4 S. Ammar, R. Abdelhedi, C. Flox, C. Arias and E. Brillas, *Environ. Chem. Lett.*, 2006, **4**, 229–233.
- 5 A. Hernández-Gordillo, V. Rodríguez-González, S. Oros-Ruiz and R. Gómez, *Catal. Today*, 2016, **266**, 27–35.
- 6 M. Cheng, G. Zeng, D. Huang, C. Lai, P. Xu, C. Zhang and Y. Liu, *Chem. Eng. J.*, 2016, **284**, 582–598.
- 7 Md. T. Uddin, M. Z. Bin Mukhlish and Md. R. H. Patwary, *Desalin. Water Treat.*, 2021, **212**, 311–322.
- 8 K. Maeda, K. Ishimaki, Y. Tokunaga, D. Lu and M. Eguchi, *Angew. Chem., Int. Ed.*, 2016, **55**, 8309–8313.
- 9 M. Shao, Y. Shao, S. Ding, R. Tong, X. Zhong, L. Yao, W. F. Ip, B. Xu, X.-Q. Shi, Y.-Y. Sun, X. Wang and H. Pan, *ACS Sustainable Chem. Eng.*, 2019, **7**, 4220–4229.



10 S. S. Wong, M. J. Hülsey, H. An and N. Yan, *Catal. Sci. Technol.*, 2022, **12**, 5217–5228.

11 S. Song, J. Qu, P. Han, M. J. Hülsey, G. Zhang, Y. Wang, S. Wang, D. Chen, J. Lu and N. Yan, *Nat. Commun.*, 2020, **11**, 4899.

12 D. R. Kumar, S. Kesavan, M. L. Baynosa, V. Q. Nguyen and J.-J. Shim, *J. Colloid Interface Sci.*, 2018, **530**, 361–371.

13 W. Dai, J. Yu, S. Luo, X. Hu, L. Yang, S. Zhang, B. Li, X. Luo and J. Zou, *Chem. Eng. J.*, 2020, **389**, 123430.

14 K. Ai, Y. Liu, J. Liu, Q. Yuan, Y. He and L. Lu, *Adv. Mater.*, 2011, **23**, 4886–4891.

15 M. Y. Malca, H. Bao, T. Bastaille, N. K. Saadé, J. M. Kinsella, T. Friščić and A. Moores, *Chem. Mater.*, 2017, **29**, 7766–7773.

16 B. Shao, X. Liu, Z. Liu, G. Zeng, Q. Liang, C. Liang, Y. Cheng, W. Zhang, Y. Liu and S. Gong, *Chem. Eng. J.*, 2019, **368**, 730–745.

17 A. Pandikumar, K. Jothivenkatachalam and S. Moscow, *Heterojunction Photocatalytic Materials*, Jenny Stanford Publishing, New York, 2022.

18 A. Galán-González, A. K. Sivan, J. Hernández-Ferrer, L. Bowen, L. Di Mario, F. Martelli, A. M. Benito, W. K. Maser, M. U. Chaudhry, A. Gallant, D. A. Zeze and D. Atkinson, *ACS Appl. Nano Mater.*, 2020, **3**, 7781–7788.

19 Y. Liu, X. Yan, Z. Kang, Y. Li, Y. Shen, Y. Sun, L. Wang and Y. Zhang, *Sci. Rep.*, 2016, **6**, 29907.

20 J. Jian, R. Kumar and J. Sun, *ACS Appl. Energy Mater.*, 2020, **3**, 10408–10414.

21 K. Kim and J. H. Moon, *ACS Appl. Mater. Interfaces*, 2018, **10**, 34238–34244.

22 W. Zhang, C. Xu, E. Liu, J. Fan and X. Hu, *Appl. Surf. Sci.*, 2020, **515**, 146039.

23 X. Wang, P. Wu, Z. Zhao, L. Sun, Q. Deng, Z. Yin and X. Chen, *J. Mater. Sci.: Mater. Electron.*, 2020, **31**, 4895–4904.

24 J. Chen, J. Zhan, E. Lu, Y. Wan, Z. Jin and H. Qi, *Mater. Lett.*, 2018, **220**, 66–69.

25 J. Chen, J. Zhan, Y. Zhang and Y. Tang, *Chin. Chem. Lett.*, 2019, **30**, 735–738.

26 H. Benhebal, C. Wolfs, S. Kadi, R. G. Tilkin, B. Allouche, R. Belabid, V. Collard, A. Felten, P. Louette, S. D. Lambert and J. G. Mahy, *Inorganics*, 2019, **7**, 77.

27 L. Liu, G. Zhao, C. Li, S. Zhou, Y. Wang and F. Jiao, *Desalin. Water Treat.*, 2021, **217**, 411–421.

28 B. Tan, Y. Fang, Q. Chen, X. Ao and Y. Cao, *Opt. Mater.*, 2020, **109**, 110470.

29 S. Bera, S. Ghosh and R. N. Basu, *New J. Chem.*, 2018, **42**, 541–554.

30 S. Jiang, K. Zhou, Y. Shi, S. Lo, H. Xu, Y. Hu and Z. Gui, *Appl. Surf. Sci.*, 2014, **290**, 313–319.

31 I. Ahmad, M. S. Akhtar, E. Ahmed and M. Ahmad, *Sep. Purif. Technol.*, 2020, **245**, 116892.

32 X. Gao, G. Huang, H. Gao, C. Pan, H. Wang, J. Yan, Y. Liu, H. Qiu, N. Ma and J. Gao, *J. Alloys Compd.*, 2016, **674**, 98–108.

33 S. Sharma and N. Khare, *Colloid Polym. Sci.*, 2018, **296**, 1479–1489.

34 H. Han, H. Choi, S. Mhin, Y.-R. Hong, K. M. Kim, J. Kwon, G. Ali, K. Y. Chung, M. Je, H. N. Umh, D.-H. Lim, K. Davey, S.-Z. Qiao, U. Paik and T. Song, *Energy Environ. Sci.*, 2019, **12**, 2443–2454.

35 Y. Liu, Y. Zhang and L. Shi, *Colloids Surf., A*, 2022, **641**, 128577.

36 X. Li, L. Youji, X. Guo and Z. Jin, *Front. Chem. Sci. Eng.*, 2023, **17**, 606–616.

37 T. V. M. Sreekanth, R. Ramaraghavulu, S. V. Prabhakar Vattikuti, J. Shim and K. Yoo, *Mater. Lett.*, 2019, **253**, 450–453.

38 H. Song, J. Sun, T. Shen, L. Deng and X. Wang, *Catalysts*, 2021, **11**, 489.

39 Q.-Y. Tang, X.-L. Luo, S.-Y. Yang and Y.-H. Xu, *Sep. Purif. Technol.*, 2020, **248**, 117039.

40 X. Zhang, L. Shi and Y. Zhang, *J. Taiwan Inst. Chem. Eng.*, 2022, **132**, 104111.

41 T. Liu, L. Shi, Z. Wang and D. Liu, *Colloids Surf., A*, 2022, **632**, 127811.

42 X. Chang, T. Wang, P. Zhang, J. Zhang, A. Li and J. Gong, *J. Am. Chem. Soc.*, 2015, **137**, 8356–8359.

43 M. I. A. Abdel Maksoud, G. S. El-Sayyad, N. Mamdouh and W. M. A. El Rouby, *J. Inorg. Organomet. Polym. Mater.*, 2022, **32**, 3621–3639.

44 D. Zhang, S. Lv and Z. Luo, *RSC Adv.*, 2020, **10**, 1275–1280.

45 R. Abdel-Aziz, M. A. Ahmed and M. F. Abdel-Messih, *J. Photochem. Photobiol., A*, 2020, **389**, 112245.

46 F. Xu, Y. Yuan, H. Han, D. Wu, Z. Gao and K. Jiang, *CrystEngComm*, 2012, **14**, 3615.

47 V. S. Kirankumar and S. Sumathi, *Mater. Res. Bull.*, 2017, **93**, 74–82.

